







Long-term field degradation of crystalline-silicon PV modules: insights from fifteen years of monitoring and forensic analysis

J.A. Tsanakas^{*} , Maxime Babics , Frédéric Mezzasalma, Alexandre Mignonac , Hervé Colin , Lionel Sicot, Philippe Marechal , Guillaume Capron, Jean-Patrice Rakotoniaina, and Jérémie Aimé 

CEA, Liten, Univ. Grenoble Alpes Campus INES, 73375 Le Bourget du Lac, France

Received: 8 November 2025 / Accepted: 12 February 2026

Abstract. This study presents a 15-yr real-field performance and degradation analysis of photovoltaic modules in a Mediterranean climate. Three technologies—polycrystalline silicon (p-Si), monocrystalline silicon, and amorphous silicon—were monitored, with a detailed forensic focus on the most severely degraded p-Si systems. The p-Si modules exhibited an average degradation rate of 2.56%/year, significantly exceeding the manufacturer’s warranty. Laboratory flash tests confirmed power losses of –33% to –70% over fifteen years. A multi-method diagnostic approach, integrating electroluminescence, ultraviolet fluorescence, lock-in thermography, and material forensics, identified two primary synergistic degradation pathways. The first involves optical losses from encapsulant yellowing, reducing current uniformly. The second, and more critical, is a severe increase in series resistance caused by interconnect corrosion and delamination, which drastically reduces the fill factor. Microcracks, while widespread, were a secondary factor. The study unequivocally links the degradation to moisture, oxygen, and light exposure, as evidenced by localized protection under a metal-backed nameplate. These findings underscore the critical discrepancy between accelerated testing and field aging, highlighting the necessity of long-term monitoring for accurate lifetime predictions and the development of more durable module materials and designs.

Keywords: PV module degradation / long-term field performance / PV module forensic analysis / PV lifetime assessment

1 Context—rationale

The sustained global growth of photovoltaic (PV) deployment over the past two decades has elevated the importance of long-term reliability, durability, and accurate lifetime performance forecasting. With PV now forming a cornerstone of decarbonization strategies worldwide, even modest deviations in long-term degradation assumptions can propagate into significant economic and energy-yield uncertainties at fleet scale. Despite remarkable advances in material science and module manufacturing, PV systems in the field are subject to complex and interacting stressors—thermal cycling, ultraviolet irradiation, humidity ingress, mechanical strain, soiling, and voltage bias—that evolve over time and interact in ways not reproducible under accelerated testing. Consequently, real-field degradation studies remain indispensable for understanding the authentic behavior of PV

technologies over time and for translating laboratory-based reliability knowledge into bankable outdoor performance expectations.

The first comprehensive evidence of real-field PV degradation emerged in the early 2000s, when King et al. [1] demonstrated that crystalline-silicon (cSi) modules exhibited diverse degradation patterns and that some module types aged significantly faster than expected. These pioneering studies prompted systematic efforts to quantify field degradation at scale. The seminal meta-analysis by Jordan and Kurtz [2] synthesized hundreds of datasets collected under varied climatic and operational conditions, revealing a median degradation rate of approximately 0.5%/year but with extreme cases exceeding 2%/year. Phinikarides et al. [3] subsequently emphasized that both intrinsic material differences and extrinsic factors—humidity, diurnal thermal swings, spectral irradiance, and mechanical loading—govern the pace of degradation. Collectively, such works established that PV degradation is not a universal or technology-invariant process but a contextual one, strongly shaped by climate, module design, mounting configuration, and maintenance regime.

* e-mail: ioannis.tsanakas@cea.fr

Beyond global statistics, detailed field analyses have revealed the diversity of degradation and failure mechanisms that arise in practice. The coordinated work of IEA-PVPS Task 13 and associated reports [4–7] established a comprehensive taxonomy of failure modes—encapsulant discoloration and browning, delamination, interconnect corrosion, solder-joint fatigue, microcracking, hot-spot formation, and potential-induced degradation (PID)—each with distinct optical, electrical, and thermal signatures. Osterwald and McMahon underscored that qualification testing, while essential, cannot replicate the combined and time-dependent stresses of real-world operation [8]. Laboratory studies have elucidated the physics and chemistry of specific mechanisms, such as boron–oxygen complex formation driving light-induced degradation (LID) in boron-doped silicon or the acetic-acid-driven corrosion processes arising from encapsulant aging, yet connecting these microscopic effects with macroscopic power loss in fielded modules remains challenging [9].

Over the past decade, the expansion of monitoring infrastructure and improved diagnostic tools have enabled a new generation of field studies that bridge outdoor performance data with component-level forensics [10–13]. Skoczek et al. [14] demonstrated significant inter-site variability in cSi module retention across European climates, while long-term investigations by Polverini et al. [15] and Dhimish et al. [16] extended the observation horizon beyond ten years, documenting technology- and site-specific degradation trajectories. More recently, studies such as those by Shaik et al. [17] in arid desert conditions, Denz et al. [18] across more than a hundred installations, and Curran et al. [19] comparing PERC and Al-BSF modules have reinforced the heterogeneity of degradation behavior and the influence of bill-of-materials quality, installation practices, and system operation.

Environmental stressors—particularly soiling, temperature extremes, and humidity—remain pivotal in shaping performance loss. The IEA-PVPS synthesis on soiling quantified annual yield reductions exceeding 10% in unmitigated arid-zone PV arrays [20], while Cordero et al. measured extreme 39% losses in the Atacama Desert [21]. Despite improvements in encapsulation and grounding, PID persists as a recurrent reliability concern: Badran et al. [22] reported that affected systems can suffer irreversible power losses exceeding 25%. The combination of electroluminescence (EL), infrared thermography (IRT), ultraviolet fluorescence (UVFL), and in-situ I - V tracing now provides powerful means for field-based diagnostics [23–26]; however, establishing quantitative relationships between visual indicators and electrical degradation is still evolving. Multi-scale case studies, such as those by Fuentes et al. [27] and Daher et al. [28], further demonstrate that inverter design, balance-of-system aging, and maintenance practices can either exacerbate or mask module-level degradation, emphasizing the inherently systemic nature of PV reliability.

Parallel efforts on emerging and thin-film technologies [7, 29–31] have expanded the understanding of degradation fingerprints beyond crystalline silicon. Long-term tropical

exposure tests of organic PV modules have shown complex humidity-driven delamination behavior, while comparative Si and CdTe field studies reveal contrasting sensitivities to moisture ingress and soiling. These results underscore that as new materials and architectures—PERC, TOPCon, heterojunction (HJT), and perovskite tandems—enter the market, sustained field validation must precede full-scale deployment. The accelerated innovation cycle of PV manufacturing now outpaces the availability of long-term reliability data, heightening the value of empirical monitoring campaigns that can inform predictive degradation models and warranty frameworks [7].

Across the accumulated literature, a clear consensus has emerged: despite extensive laboratory and short-term outdoor knowledge, long-duration, technology-comparative field datasets that integrate continuous monitoring with systematic laboratory forensics remain scarce. Most available studies are limited to specific climates or fewer than ten years of exposure, constraining the generalization of degradation models and limiting insight into slow-acting mechanisms. The scarcity of such datasets hinders not only the validation of predictive lifetime models but also the calibration of warranty and risk-assessment frameworks that underpin the bankability of large-scale PV investments [32, 33]. As the global PV fleet matures, there is an urgent need for comprehensive empirical studies that couple environmental monitoring, electrical performance analysis, and material-level diagnostics over decadal timescales.

Responding to this need, the present work provides a rare fifteen-year field dataset obtained at CEA’s outdoor PV test site in Cadarache, southern France. Three distinct technologies—polycrystalline silicon (p-Si), monocrystalline silicon (m-Si), and amorphous silicon (a-Si)—have been operated under identical electrical and environmental conditions characteristic of a Mediterranean climate. Continuous monitoring of irradiance, temperature, and electrical parameters is complemented by periodic diagnostic campaigns employing I - V flash testing, infrared imaging, and EL, as well as laboratory investigations of selected aged modules. The objective is to quantify long-term degradation rates, identify dominant aging signatures, and relate field-observed performance loss to the underlying physical and material mechanisms. By coupling one of the longest operational datasets of its kind with detailed post-exposure forensics, this study delivers technology-comparative evidence essential for refining degradation models, validating predictive lifetime tools, and informing both manufacturers and asset operators. Although analogous campaigns exist in other climatic regions, each long-term dataset provides unique insight into the interplay between design, environment, and degradation behavior. The findings presented here therefore contribute to the global understanding of PV reliability, offering benchmark data for model validation and supporting the ongoing refinement of durability standards and predictive yield methodologies. The following section details the experimental configuration and methodology of this fifteen-year investigation.

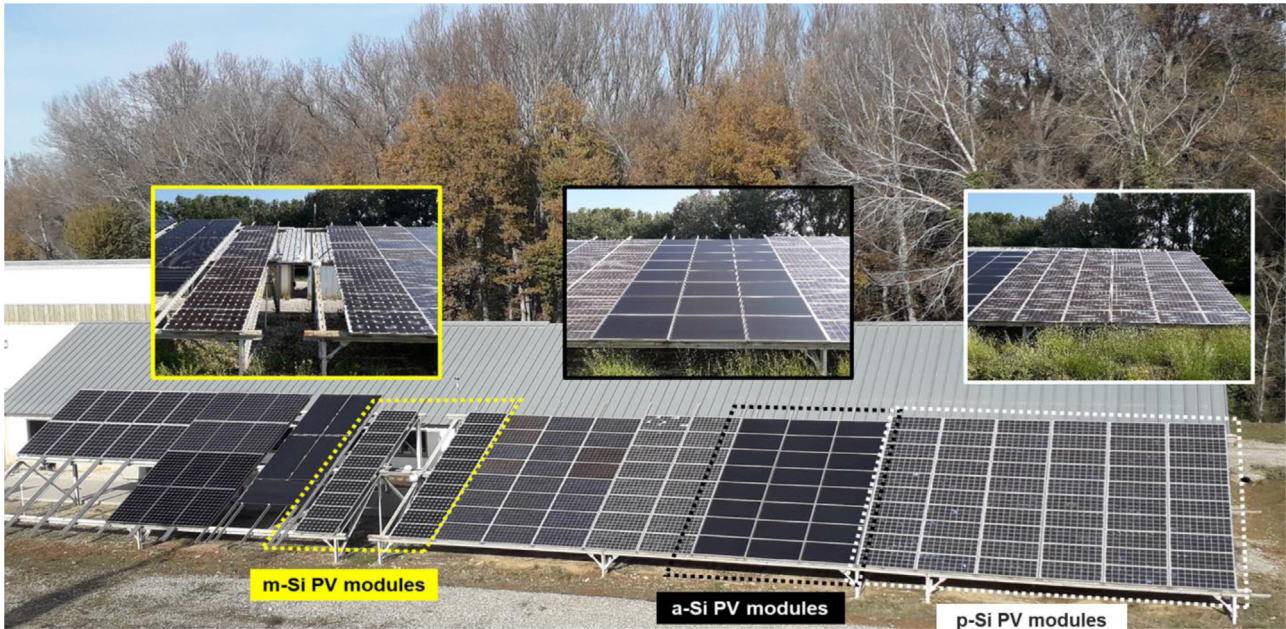


Fig. 1. Overview of the studied PV test arrays installed in Cadarache site.

2 Methodology—experimental setup

2.1 The studied PV system—field monitoring

The study was conducted at the CEA outdoor test facility in Cadarache, located in southern France (44.06° N, 5.46° E). This region experiences a Mediterranean climate characterized by high annual solar insolation (approximately 1700 kWh/m²/year), hot, dry summers, and mild, humid winters. Key climatic stressors relevant to PV degradation at this site include significant diurnal and seasonal thermal cycling, high summer operational temperatures often exceeding 45°C, substantial ultraviolet (UV) exposure, and seasonal humidity. This specific climate profile, with its combined thermal, UV, and moisture stresses, provides an accelerated yet realistic aging environment, representative of many temperate and semi-arid regions with high PV deployment.

Three grid-connected 1 kWp PV systems, based on p-Si, m-Si, and a-Si technologies, were installed in a fixed, open-rack configuration at a standard tilt angle of 30° facing due south. The systems have been in continuous operation since their commissioning in 2008. Each array is connected to a dedicated SMA Sunny Boy SWR1100E string inverter, with a nominal efficiency of 95.2%. The specific p-Si modules under detailed investigation in this study are of a vintage design, comprising 36 series-connected cells (nominal power: 75 Wp) packaged with an ethylene-vinyl acetate (EVA) encapsulant and a polyvinyl fluoride (PVF)/polyethylene terephthalate (PET)/PVF (TPT) backsheet. Figure 1 provides an overview of the studied PV arrays in the Cadarache PV test site.

A comprehensive, high-precision monitoring station was deployed to capture synchronized environmental and electrical data. Global Horizontal Irradiance and Plane of Array irradiance are measured using secondary standard

Kipp & Zonen CMP11 pyranometers, calibrated biennially. The spectral response and in-situ current of the PV technologies are monitored using c-Si and a-Si reference cells.

Module temperature is measured using PT100 platinum resistance thermometers (accuracy $\pm 0.1^\circ\text{C}$ at 0°C) attached to the backsheet at the center of selected modules. Ambient temperature and relative humidity are logged with a ventilated and radiation-shielded sensor. Wind speed and direction are recorded at a height of 3 meters using a cup anemometer and wind vane.

All critical electrical parameters—including DC voltage (V_{dc}) and current (I_{dc}) from the array, and AC power (P_{ac}) and energy fed into the grid—are measured by high-accuracy transducers and logged by a Campbell Scientific CR1000 data logger at 5-min intervals. This high-resolution dataset enables the calculation of key performance indicators such as the final yield (Y_f), reference yield (Y_r), and the performance ratio (PR), which normalizes the actual energy output against the theoretical potential, providing a weather-independent metric for degradation analysis.

Periodic auxiliary infrared (IR) imaging surveys have been conducted using a FLIR T640bx thermal camera to identify and document thermal anomalies such as hot spots caused by cracked cells, defective bypass diodes, or faulty interconnects.

2.2 Laboratory characterization

To deconvolute the root causes of performance degradation, a subset of modules, with a primary focus on the severely degraded p-Si technology, was retrieved for detailed laboratory forensics at CEA-INES. The multi-technique characterization campaign was designed to correlate macroscopic power loss with microscopic material and electrical failures.

***I*–*V* characterization:** Current-voltage (*I*–*V*) curves were measured under Standard Test Conditions (STC: 1000 W/m², AM 1.5 G spectrum, 25°C cell temperature) using a class A+ Spire 5600 SPL flash solar simulator. The system’s spectral match is better than ±12.5% of the required intervals per IEC 60904-9, and spatial non-uniformity is less than ±2%. To investigate performance under real-world operating conditions, *I*–*V* curves were also acquired at controlled irradiance levels of 200, 400, 600, and 800 W/m². Parameters such as I_{sc} , V_{oc} , P_{max} , FF, series resistance (R_s), and shunt resistance (R_{sh}) were extracted for analysis.

Electroluminescence (EL) imaging: EL imaging was performed using a high-sensitivity, Peltier-cooled GreatEyes CCD camera. To probe different aspects of module health, images were captured at multiple current injection levels: a low injection of 1 A (approximately 25% of I_{sc}) to identify series resistance limitations and shunts, and a high injection of 6 A (approximately 150% of I_{sc}) to overcome the high series resistance of degraded modules and visualize cracked and inactive cell regions. The integration time was adjusted accordingly, up to 30 s for the most degraded samples.

Dark lock-in thermography (DLIT): For high-resolution defect localization, DLIT was performed using an in-house system. The module under test was placed in a dark enclosure and periodically excited by a pulsed, high-power, spectrally tunable LED array. The thermal response was measured synchronously using a cooled mid-wave infrared camera (FLIR Phoenix, InSb detector, 3–5 μm). The lock-in technique isolates the Joule heating signature of specific defects, enabling the quantitative mapping of local shunts, series resistance hotspots, and micro-cracks with a thermal resolution of <20 mK.

Ultraviolet Fluorescence (UVFL) imaging: UVFL imaging was employed to study the photodegradation of the EVA encapsulant. A high-power UV torch (DARKDAWN) with a peak emission at 365 nm and a power of 1.3 W was used for excitation. The resulting fluorescence from the polymer was captured with a digital camera. This technique visually maps the distribution of fluorescent chromophores (polyenes) formed during EVA aging, with photobleached areas indicating regions of oxidative degradation.

Material and chemical forensics: A destructive analysis was conducted on selected modules. Visually inspected samples were documented for physical defects. The encapsulant was carefully dissected for further analysis:

- **Fluorescence spectroscopy:** Emission spectra of the EVA were measured using a Hitachi F-4500 fluorescence spectrophotometer with a 150 W Xe lamp. Spectra were recorded from 400 to 800 nm with an excitation wavelength of 360 nm and a slit width of 5 nm.
- **UV-Vis spectroscopy:** Optical transmission spectra of the encapsulant samples were acquired in the 300–1200 nm range using a PerkinElmer L950 spectrophotometer with a resolution of 10 nm per step. This was used to calculate the yellowness index (YI) according to ASTM E313.

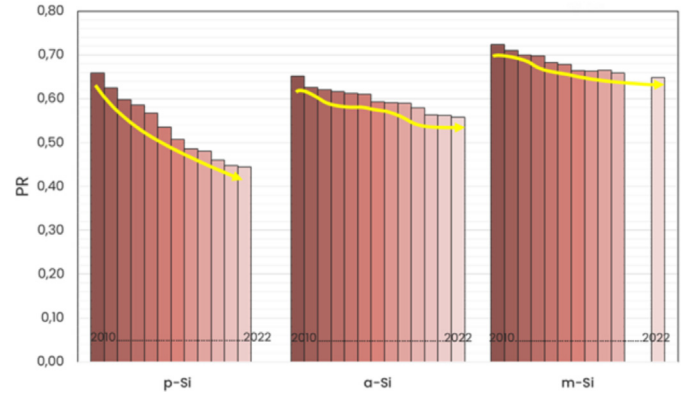


Fig. 2. Evolution of PR for the studied modules (2010–2022).

- **Fourier-transform infrared (FTIR) spectroscopy:** Chemical bonding changes were analyzed using a Thermo Scientific Nicolet 6700 FT-IR spectrometer equipped with a Diamond ATR (Attenuated Total Reflectance) accessory. Spectra were recorded over 32 scans with a resolution of 4 cm⁻¹ in the range of 4000–525 cm⁻¹. The ATR crystal was rigorously cleaned with isopropyl alcohol between measurements to prevent cross-contamination.

This holistic, multi-scale methodology—spanning from system-level outdoor monitoring to component-level material forensics—ensures a robust and comprehensive understanding of the long-term degradation mechanisms.

3 Results and discussion

3.1 “Macroscopic” analysis: performance degradation trends

To quantify long-term performance degradation, annual degradation rates were derived from the evolution of the PR over time. The PR time series for each technology was analyzed over the monitoring period (2010–2022), and a linear regression was applied to determine the temporal trend. The slope of the fitted line was then normalized to the initial PR value and expressed in %/year. This approach provides a weather-corrected and technology-consistent metric of degradation, ensuring comparability across module types and methodological transparency.

The overall results from the field-monitored data indicate significant performance degradation for the p-Si modules, with an average degradation rate of 2.56%/year. This value is considerably higher than the 0.6–0.8%/year degradation rate specified by the manufacturer. In contrast, the m-Si and a-Si modules exhibited lower degradation rates (0.86%/year and 1.15%/year, respectively), with the m-Si technology demonstrating superior long-term stability (Fig. 2).

Comparative *I*–*V* curve measurements taken at the beginning of the monitoring period (2008) and at the end (2023) revealed substantial reductions in current output for the whole string of the p-Si modules (Fig. 3, left).

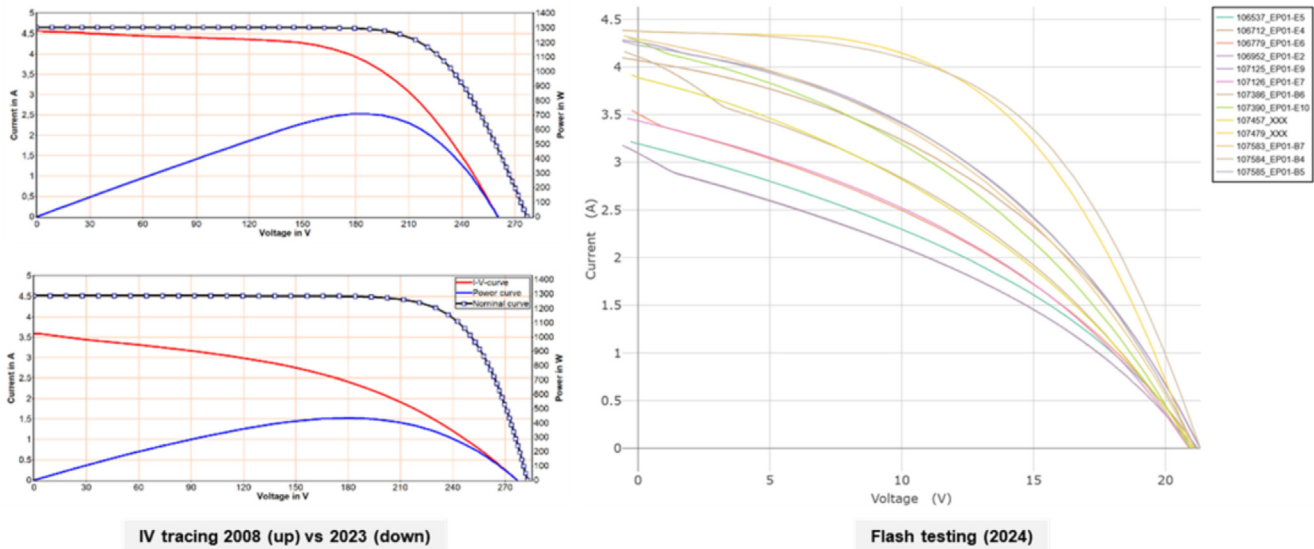


Fig. 3. Left: Comparative results (2008 vs. 2023) of IV tracing for the p-Si modules' string. Right: Consolidated results of indoor flash tests (I - V characterization) for all fielded p-Si modules.

Laboratory flash tests (Fig. 3, right) confirmed these findings, quantifying power losses ranging between -33% and -70% over the 15-year period. These losses suggest contributions from both intrinsic material degradation and external environmental factors. Quantitatively, the power loss is driven by a significant drop in the maximum power (P_{mpp}), FF , and current at maximum power (I_{mpp}), with reductions of up to -41% , -36% , and -27% , respectively. These electrical parameter shifts are in direct correlation with a substantial increase in R_s , which rose by up to 2.6 times its initial value, while the R_{sh} decreased by up to 5.4 times.

Before proceeding to the forensic-level analyses, it is important to clarify the rationale for concentrating this part of the study on the p-Si technology. Among the three module types monitored in this campaign, p-Si was selected for in-depth investigation because it exhibited the highest and most heterogeneous degradation. This technology, representative of the mainstream PV generation deployed in the late 2000s, offers a meaningful benchmark for legacy-module reliability under realistic stress conditions. Its higher grain-boundary density, conventional EVA/TPT laminate structure, and early-generation metallization make it particularly vulnerable to moisture ingress, encapsulant discoloration, and interconnect corrosion. For these reasons, p-Si provides an ideal case study for identifying degradation mechanisms that are both historically relevant and instructive for current and emerging PV designs.

3.2 In-depth assessment: forensics-based analysis

The forensic diagnostics presented in this work primarily concern the post-exposure retrieval of modules after fifteen years of field operation (T_{final}). While continuous electrical monitoring (PR, DC parameters, and energy yield) and ad hoc field measurements (IV tracing, IR thermographic, and visual inspections) were performed throughout the operational period, intermediate laboratory-based forensic

campaigns were not conducted. The present analysis therefore focuses on the characterization of the aged state and the identification of cumulative degradation mechanisms resulting from long-term real-field exposure.

3.2.1 Analysis of I - V parameters (population study)

Figure 4 shows the distribution of the I - V parameters for the 14 field-aged modules, compared with the nameplate specifications. The module nameplates indicate a V_{oc} of 21.5 V, an I_{sc} of 4.7 A, a calculated FF of 0.74, and a P_{max} of 75 W, corresponding to a cell efficiency of approximately 13.3% under one-sun illumination.

After fifteen years of outdoor operation, the average V_{oc} was measured at 21.12 V, indicating that this parameter remained remarkably stable. In contrast, the I_{sc} exhibited a wide distribution, ranging from 4.37 A down to 3.00 A. This corresponds to current losses between 7% and 36% relative to the nominal value. Regarding the FF , most modules displayed severely degraded performance, with values clustered between 36% and 42%. Only two modules exhibited slightly higher FF values of 53.3% and 53.9%, respectively. This represents a reduction of 27% to 54% compared to the nominal FF . Consequently, the P_{max} followed a similar trend, ranging from 22.7 W to 50.3 W, significantly below the initial rated power of 75 W. Overall, the modules experienced power losses between 33% and 70% under standard test conditions. The observed performance dispersion was unexpected and, assuming the absence of specific external degradation events, may indicate inconsistencies in the manufacturing quality control, suggesting that one or more production steps or components were insufficiently controlled during fabrication.

To investigate the differences in module performance—particularly in I_{sc} and FF —two modules (Module 4 and Module 14, indicated by arrows in Figure 4d) were selected for in-depth analysis. These modules represent

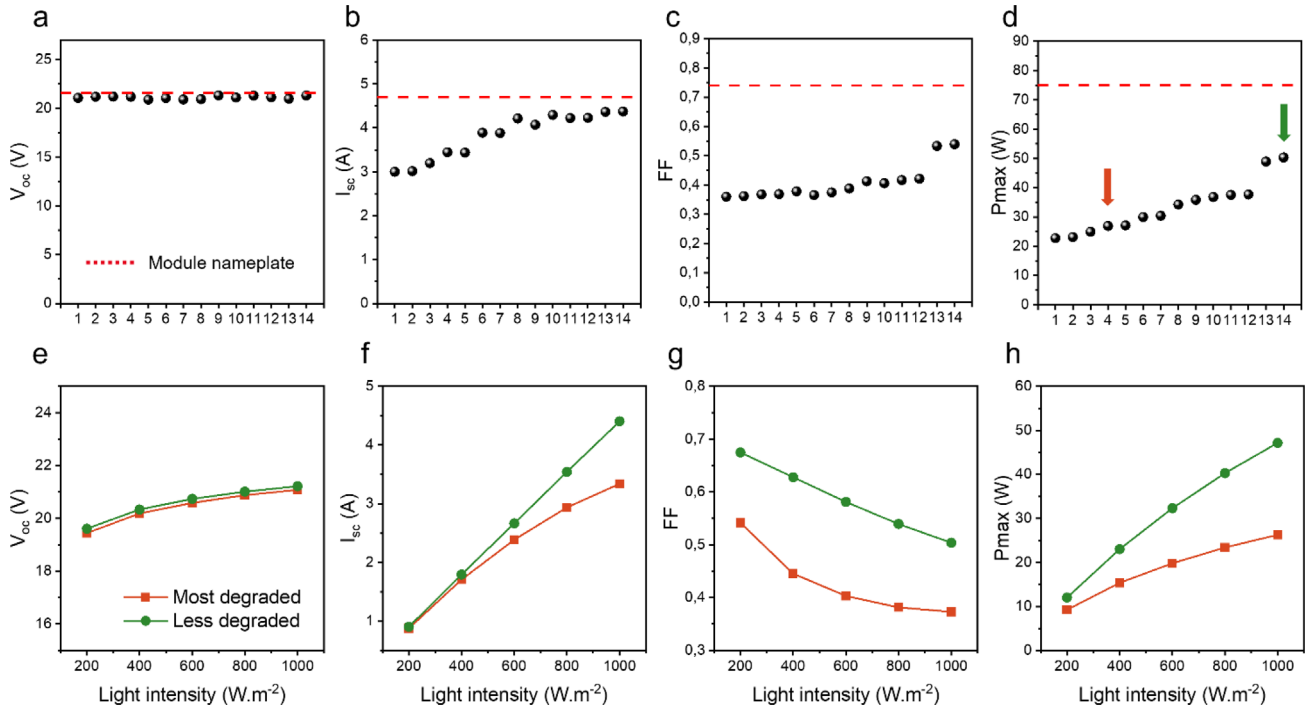


Fig. 4. Distribution of the I - V parameters of 14 modules after field aging: (a) V_{oc} , (b) I_{sc} , (c) FF , and (d) P_{max} . Light dependence of the I - V parameters on 2 selected modules, representatives of the most and the less degraded: (e) V_{oc} , (f) I_{sc} , (g) FF , and (h) P_{max} .

the least and most degraded samples, respectively. The current-voltage (I - V) characteristics were measured under varying illumination levels, from 200 W/m^2 to 1000 W/m^2 , to assess the influence of series resistance at different current densities.

The dependence of V_{oc} on light intensity exhibited a typical semi-logarithmic behavior for both modules, with no abnormal trends. For the less degraded module, I_{sc} increased linearly with illumination, as expected, showing no significant deviation other than a uniform reduction across all light intensities. This uniform reduction is attributed to a constant optical loss, primarily from encapsulant yellowing, which is discussed in detail in the following section. In contrast, the most degraded module showed a clear deviation from linearity in the I_{sc} -illumination relationship, with notably lower I_{sc} values at higher irradiance levels. This behavior is characteristic of high series resistance, which hinders efficient current collection at elevated current densities.

For both modules, the FF decreased substantially as illumination increased, a trend that was even more pronounced in the most degraded module. This strong dependence of FF on irradiance further supports the presence of significant series resistance losses. As a result, the maximum power output (P_{max}) followed a nonlinear trend with increasing illumination for both modules, reflecting the combined effects observed in the I - V parameters.

Overall, two main degradation mechanisms can be identified: (1) optical losses due to encapsulant yellowing, which uniformly reduces light transmission across all irradiance levels, and (2) electrical losses caused by

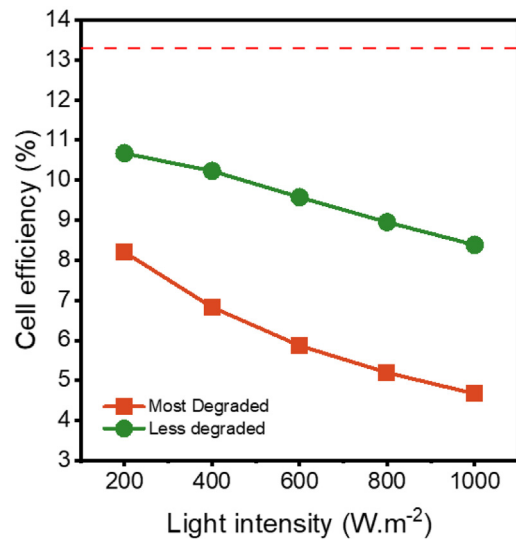


Fig. 5. Calculated cell efficiency at different light intensities for the most and the less degraded module. The nameplate calculated efficiency under 1 sun illumination of 13.3% is indicated as a reference.

increased series resistance, which limits current extraction and reduces the FF , especially under high illumination. Finally, although module performance is significantly reduced under standard test conditions (1 sun), the loss in efficiency is less severe at lower irradiance levels (Fig. 5). This irradiance-dependent behavior could explain why the annual energy yield losses observed in the field are less pronounced than the degradation measured under STC in the laboratory.

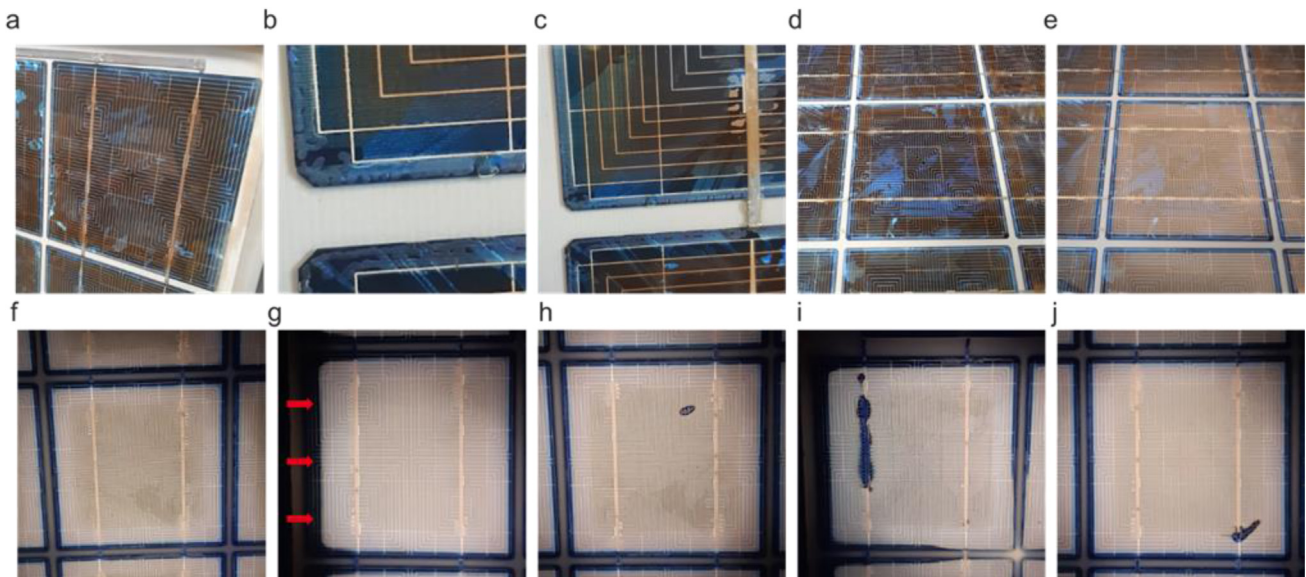


Fig. 6. Visual and UVFL inspection of the module. (a) Detail of the module corner. (b) Delamination visible at the edges of the cells. (c) Delamination visible near the soldering points. (d) Discoloration of the encapsulant. (e) Same area illuminated with a UV torch with an emission of 365 nm. (f) Typical pattern observed under UVFL. (g) Cell located on the side of the module. (h) Small crack in the middle of the cell. (i) Crack along the busbar. (j) A crack starting from the busbar that extends to the cell.

3.2.2 Visual inspection and correlation with UVFL imaging

A typical cell from a module is presented in Figure 6a. All cells from all examined modules exhibited signs of delamination along the cell edges, as depicted in Figure 6b. This is likely attributable to changes in the mechanical properties of the encapsulant induced by the combined effects of moisture ingress and prolonged light exposure, as discussed later. In the most degraded modules, we also observed several delamination areas near the soldering points along the busbars (Figure 6c). This additional degradation could result in a weaker electrical contact between the busbar and the cell or local corrosion due to the presence of air. Both scenarios would explain, at least partially, the higher series resistances measured in the most degraded modules.

All modules also showed noticeable discoloration, characterized by yellow and brown areas. Since encapsulant yellowing is commonly associated with the formation of fluorescent chromophores, a UV lamp with an excitation wavelength of 365 nm was used to reveal their presence or absence, as illustrated in Figures 6d and 6e [34,35]. The observed fluorescence pattern (Figure 6f) corresponds to a well-documented phenomenon, where fluorescence appears over most of the encapsulant surface except in the intercell regions [36]. In these intercell areas, the ingress of moisture and oxygen through the backsheets, combined with light exposure, leads to photobleaching of the yellow chromophores as they form.

Beyond this general pattern, photobleaching proved useful for identifying additional degradation mechanisms, such as localized moisture ingress and cell cracking. In the latter case, oxygen diffusion through cracks to the cell front

surface induces localized photobleaching, resulting in non-fluorescent regions. Figure 6g shows a cell located at the module edge, where enhanced moisture and oxygen penetration from the sides caused deeper photobleaching of the yellow chromophores. Figure 6h highlights a microcrack, while Figure 6i presents a large crack propagating along the busbar, likely associated with the module interconnection process. Due to the multicrystalline nature of the wafers, these cracks do not follow the typical (100) crystallographic plane observed in modern monocrystalline cells. The extent of the photobleached region—comparable to that observed at the intercell areas—suggests that this particular crack probably originated during module fabrication. Because the crack lies beneath the interconnection ribbon, it would likely remain undetected in standard EL imaging, underscoring the complementary diagnostic value of UVFL imaging. Another example (Figure 6j) shows a crack that probably originated during the soldering process.

Interestingly, all modules exhibited at least one intercell region showing visible yellowing of the encapsulant (Figures 7a and 7b), in contrast to the photobleached appearance of the rest of the module's intercell areas (Figures 7c and 7d). This localized yellowing coincides with the position of the nameplate sticker on the module backside, which incorporates an aluminum layer for durability. This metal layer provides enhanced local protection against moisture and oxygen ingress. Notably, in this specific, protected region, no delamination was observed at the cell corners (Figure 7c). This finding highlights the synergistic role of moisture, oxygen, and light in driving both encapsulant delamination and the chemical changes leading to yellowing or photobleaching.

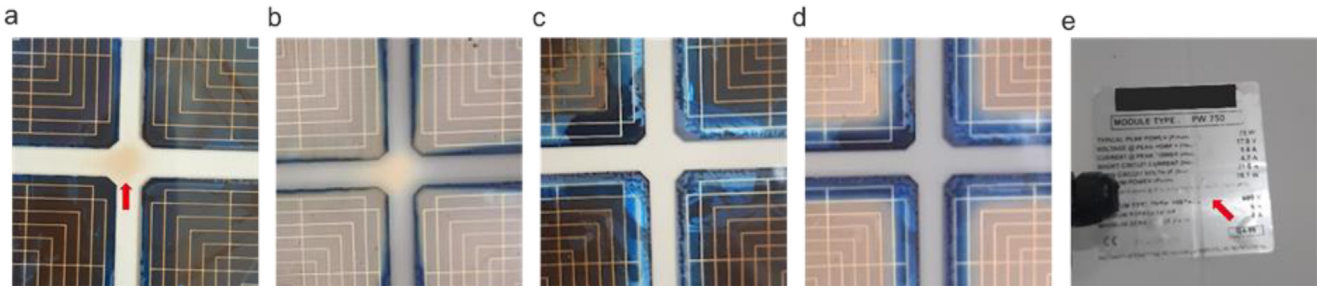


Fig. 7. (a) Specific intercell region where encapsulant yellowing is preserved. (b) The same region under 365 nm UV illumination, showing reduced photobleaching. (c) Typical intercell region without preserved yellowing. (d) The same typical region under 365 nm UV illumination, exhibiting photobleaching due to oxygen ingress. (e) Backside view of the module showing the aluminum-backed nameplate corresponding to the preserved yellowing location. Red arrows indicate the matching front-side and back-side positions.

This observation also suggests a potential durability benefit of modern backsheets that incorporate an aluminum moisture barrier within their multilayer structure.

3.2.3 Component-level analysis

To better quantify the extent of yellowing and its impact, a partial destructive analysis was performed on one module. During this process, a large portion of the front-side encapsulant was successfully removed due to its weak adhesion to both the solar cell and the cover glass. In contrast, removal of the backside encapsulant was not possible because of its strong adhesion to the backsheet and the cell. While the front encapsulant could be detached in a single large piece (Figures 8a and 8b), the material at the intercell regions exhibited poor mechanical integrity and disintegrated into multiple fragments. Consequently, the recovered encapsulant contained limited portions of the photobleached areas typically found near the cell edges. During the destructive procedure, a strong acetic acid odor was detected, indicating its formation and retention within the module during field operation. The presence of acetic acid is consistent with the known hydrolysis degradation pathways of EVA encapsulants.

Fluorescence spectroscopy and optical transmission measurements were then performed on different locations of the recovered encapsulant. The fluorescence emission spectra (Figure 8c), obtained under 360 nm excitation, are shown for Positions 1 and 7 (as defined in Figure 8b). For position 7, the emission peaked at 587 nm, whereas for position 1 it was slightly more intense and peaked at 600 nm. These emission characteristics align with previous reports on EVA discoloration, which indicate that both the emission intensity and wavelength increase over time due to the formation and growth of conjugated polyenes in the degraded EVA [34]. The transmission spectra from the different locations of the recovered encapsulant are presented in Figure 8d and are also compared with a modern, non-aged EVA encapsulant film for reference. The aged encapsulant's transmission is strongly reduced, especially in the 300–600 nm spectral region. The data confirm the visual impression; the most browned encapsulant at Position 1 has the lowest transmission. For the

rest of the encapsulant covering most of the solar cell, from Position 3 to Position 7, the transmission spectra are identical, showing a significant reduction compared to the reference.

From the transmission spectra, we extracted both the average optical transmittance (300–1200 nm) and the yellowness index, calculated according to IEC 62788-1-4; the results are presented in Figure 8e. The yellowness index reached values up to 27 at Position 1 and decreased to approximately 10 across the rest of the film (Positions 3–7). Correspondingly, the average transmittance was 74% at the cell edge (Position 1) and about 82% for Positions 3 to 7. These average transmission values are provided as indicative metrics, as they do not fully capture the wavelength-dependent nature of the optical losses. Moreover, the exact impact on the I_{sc} also depends on the cell's spectral quantum efficiency, which was not possible to measure in this study. For comparison, the reference encapsulant exhibited an average transmittance of approximately 92%. Overall, the reduction in average optical transmittance within the aged encapsulant accounts for the observed decrease in I_{sc} for the less degraded modules (e.g., Modules 8 to 14).

Finally, we investigated potential chemical degradation using FTIR spectroscopy. The results for Location 1, Location 7, and a sample from the intercell area are presented in Figure 8f. The FTIR spectra are typical for an EVA polymer; however, an additional feature appears between 1500 and 1650 cm^{-1} for Locations 1 and 7, as indicated by the arrow. This spectral region has been associated with the presence of carbonyl ($\text{C}=\text{O}$) and carbon-carbon double bonds ($\text{C}=\text{C}$) following the formation of ketones, aldehydes, esters, or carboxylic acids [37,38]. The absence of this peak in the sample from the photobleached intercell area could indicate that these volatile compounds diffused out of the module over time, as previously hypothesized [38]. The volatile nature of these compounds could also explain an observed experimental artifact: during initial FTIR measurements, this peak would systematically increase from one measurement to the next, likely due to the contamination of the ATR equipment and the release of the compounds upon contact, which led to unreliable results until a rigorous cleaning protocol was implemented between each measurement.

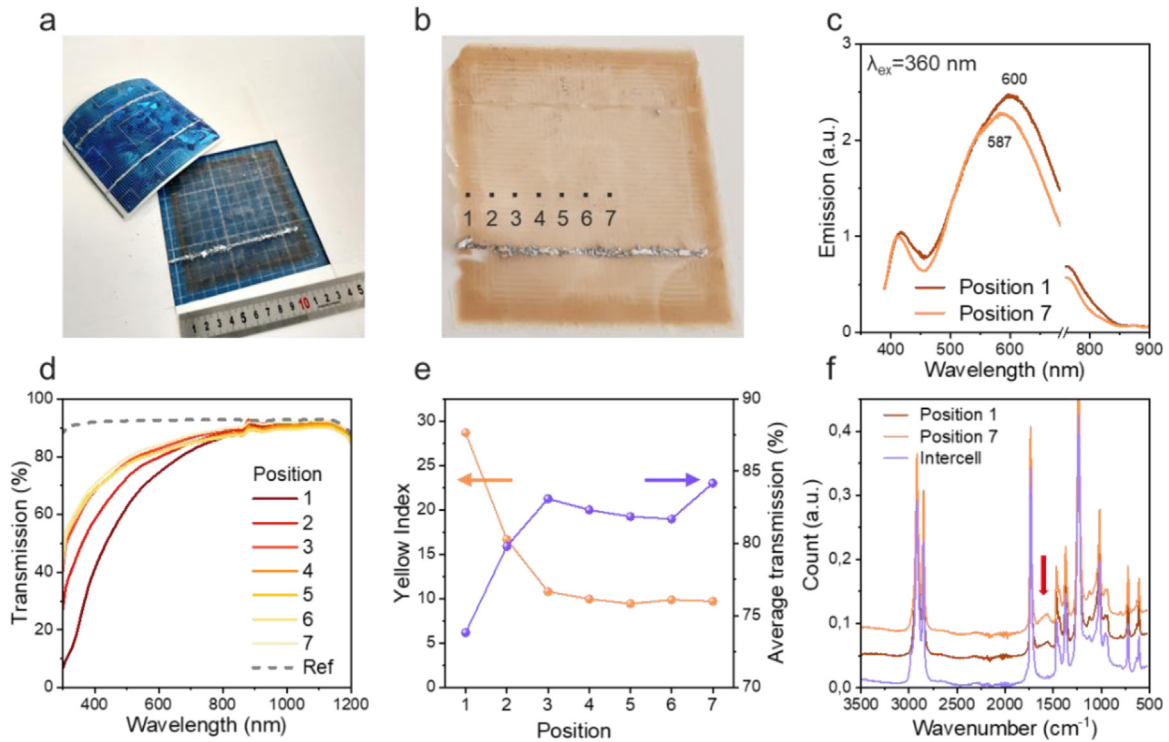


Fig. 8. (a) Photography of the backsheet/encapsulant/cell stack removed from the front encapsulant/glass stack. (b) Photography of the front encapsulant removed from the front glass with different positions indicated. (c) Emission spectra of the encapsulant excited at 360 nm. (d) Transmission spectra from the various positions. A non-aged laminated modern EVA film is given as a reference. (e) Yellow index and average transmission extracted from the transmission spectra. (f) FTIR spectroscopy from the various positions.

3.2.4 Comparative analysis of EL, UVFL, and DLIT signatures

To further investigate the performance differences between the two degraded modules, we performed a comparative analysis using EL, UVFL, and DLIT.

For the most degraded module, EL measurements required a high current injection (6 A) to obtain a sufficient signal-to-noise ratio. The resulting EL image (Figure 9b) shows strong luminescence along the cell edges and busbars, while the central regions of the cells exhibit much weaker emission, appearing dark. At lower injection currents, the EL signal was too noisy to be exploitable. The reconstructed UVFL image (Figure 9c) reveals that 12 out of 36 solar cells exhibit cracks, predominantly located along the busbars. Several of these cracks correspond to regions of enhanced EL brightness, suggesting significant local current flow and recombination at these defective sites. DLIT images (Figure 9d) reveal two distinct types of hotspots. The first type coincides with the cracks observed in UVFL and the bright regions in EL, typically located along the busbars. The second type appears at the intersections between cell edges and busbars—specifically, at the interconnections where the busbar transitions from the rear of one cell to the front of the next. In this module technology, each cell with two busbars is soldered to its neighbor. Fatigue, corrosion, and changes in the mechanical properties of the encapsulant could have weakened these soldering points over time. Consistent with the EL results, the central regions of the cells remain dark in DLIT,

indicating that the injected current poorly reaches these areas due to high series resistance or local disconnections within the current collection path.

In contrast, the less degraded module exhibits markedly different behavior. The EL image acquired at 6 A (Figure 9e) shows a more uniform emission across the cell surface, with only slightly brighter regions along the busbars. This pattern is consistent with the I - V measurements under varying illumination, which showed better current extraction at high irradiance levels for this module. Interestingly, one cell located near the bottom-left corner of the module displays an EL signature similar to that of the most degraded module, with bright edges and a dark center. This observation suggests that this particular cell is in a more advanced state of degradation and that further aging of the entire module could lead to similar widespread performance losses. Low-injection EL (1 A) imaging (Figure 9f) was possible for this module due to its overall lower series resistance, but it did not reveal any additional features not seen at 6 A. UVFL imaging (Figure 9g) indicates that 22 out of 36 cells exhibit cracks—substantially more than in the most degraded module. This observation corroborates previous studies showing no direct correlation between the number of cracks and overall module performance, emphasizing that the *type* and *electrical impact* of defects are more critical than their mere quantity. DLIT images (Figure 9h) also display a distinct thermal signature: most hotspots are located within the cells along the busbars, but they do not necessarily align with all the cracks identified by UVFL. Moreover, the central regions of the cells exhibit

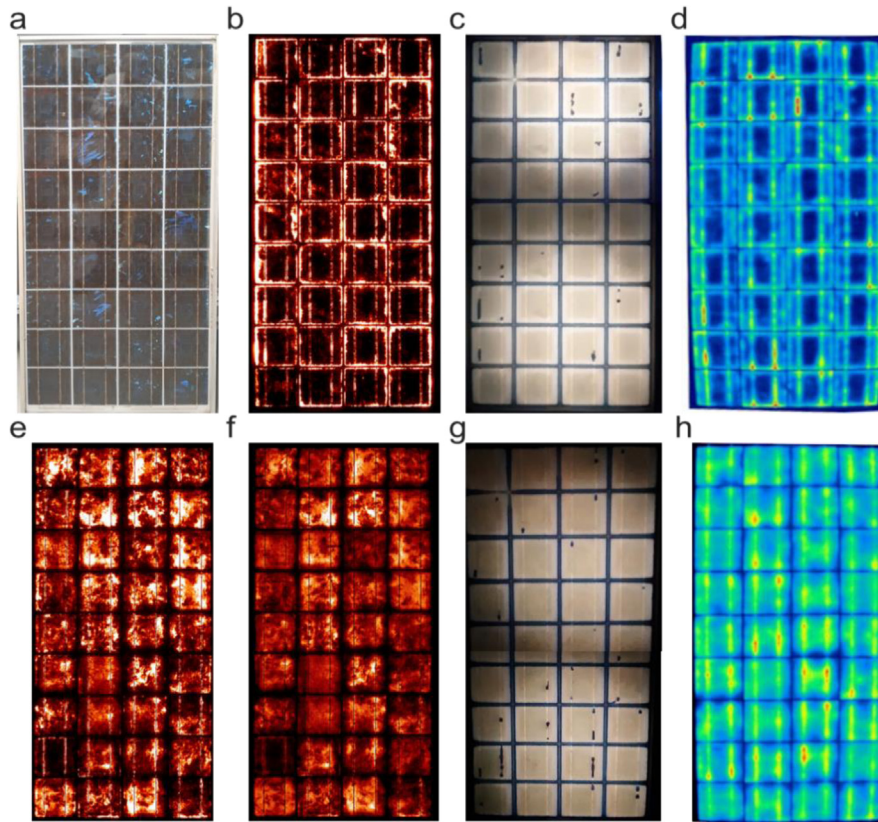


Fig. 9. (a) Photography of a typical module after field aging. (b) EL image of the most degraded module at 6A current injection. (c) UVFL image (reconstructed) of the most degraded module. (d) Lock-in thermography of the most degraded module. (e) EL image of the less degraded module at 6A current injection. (f) EL image of the less degraded module at 1A current injection. (g) UVFL image (reconstructed) of the less degraded module. (h) Lock-in thermography of the less degraded module.

a stronger and more uniform thermal response than in the severely degraded module, suggesting that current transport through the bulk of the cell remains relatively effective.

3.3 Connecting the dots: degradation storyline

The multi-scale evidence collected over fifteen years allows the reconstruction of a coherent degradation narrative for the studied polycrystalline-silicon modules. Field performance, I - V characteristics, imaging diagnostics, and chemical forensics converge toward a two-pathway degradation model, illustrated schematically in Figure 10, which summarizes how optical and electrical mechanisms evolve and interact over time.

At the macroscopic level, the modules experienced an average annual degradation rate of about 2%/year, leading to power losses far beyond warranty expectations. The progressive drop in I_{sc} and FF cannot be explained by isolated mechanisms; instead, it results from the combined action of optical attenuation and electrical impedance growth within the laminate stack.

The first pathway is optical in nature. The formation of conjugated polyenes and carbonyl species within the EVA encapsulant, evidenced by the fluorescence red-shift (600 nm emission) and FTIR carbonyl peaks, reduces light

transmission, particularly in the blue-green spectral region. This translates to a nearly uniform decrease in I_{sc} across illumination intensities, consistent with the “uniform current reduction” observed during I - V sweeps. Optical losses alone, however, cannot account for the severe FF collapse.

The second pathway, electrical and far more detrimental, stems from encapsulant hydrolysis and acetic-acid release. These processes promote interconnect corrosion, busbar/encapsulant delamination, and the formation of local high-resistance zones, as confirmed by DLIT hotspots and EL dark areas. The ensuing rise in series resistance—by a factor of ≈ 2.6 —creates a non-linear degradation response: power loss accelerates at high irradiance, where current density amplifies resistive drops. This irradiance-dependent behavior aligns with field observations of less severe annual yield losses compared with standard-test conditions, since modules spend much of the year operating below one-sun intensity.

Environmental exposure modulates both pathways. The observation that the small area shielded by the aluminum-backed nameplate remained free of delamination and yellowing provides direct evidence that moisture, oxygen, and light act synergistically to drive both the chemical and mechanical degradation. Even limited diffusion barriers can substantially retard aging, validating

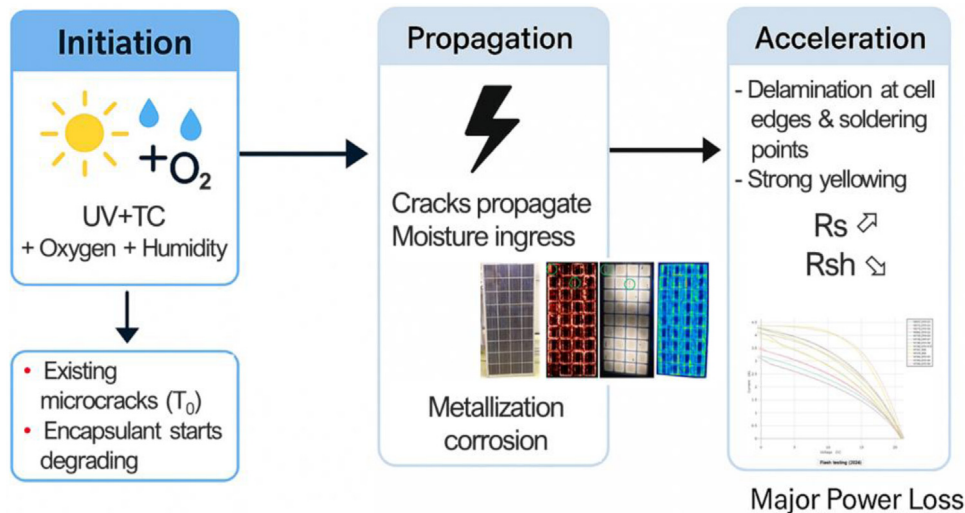


Fig. 10. Schematic representation of the integrated degradation storyline for the studied p-Si modules after 15 yr of field exposure. The diagram illustrates the two dominant and interacting pathways: (i) optical attenuation caused by photo-oxidation and yellowing of the EVA encapsulant, leading to uniform short-circuit current losses, and (ii) electrical resistance growth driven by acetic-acid-induced corrosion and delamination at interconnects, resulting in severe fill-factor reduction. Environmental stressors—light, heat, and moisture—initiate encapsulant hydrolysis, while localized protection under the aluminum-backed nameplate highlights the mitigating effect of moisture and oxygen barriers.

the durability improvements achieved in modern modules that incorporate aluminum-based or fluoropolymer barriers in their backsheets.

Taken together, these findings reveal a systemic degradation process rather than isolated defects. Microcracks, although numerous, exert only a secondary influence under these conditions. Instead, the interrelation between encapsulant chemistry, interconnect integrity, and environmental permeability governs the long-term reliability of the laminate. The conceptual synthesis presented in Figure 10 summarizes this interaction chain—from environmental exposure through encapsulant degradation to optical and electrical performance loss—illustrating how macroscopic power decline emerges from microscopic material transformations. This integrative perspective reinforces the broader industry challenge highlighted in the introduction: standard accelerated tests underestimate the coupled thermo-photo-hydrolytic stresses present in real climates. Bridging this gap requires long-duration field datasets like the present one to calibrate both predictive lifetime models and qualification protocols.

It is important to emphasize that the stronger degradation observed in the p-Si technology should not be interpreted as an intrinsic limitation of p-Si itself. The three technologies investigated originate from different manufacturers and correspond to distinct generations of module design and BOM. The p-Si modules represent an early-generation laminate architecture based on EVA encapsulation and TPT backsheets, whereas the m-Si modules exhibit different laminate configurations and material stacks. The degradation mechanisms identified here—encapsulant hydrolysis, acetic-acid-driven interconnect corrosion, and moisture ingress—are therefore primarily laminate- and material-driven rather than solely determined by cell crystallography.

The observed degradation should therefore be understood as the result of multiple interacting factors, including laminate architecture, interconnection design, manufacturing strategy, and cell technology. While encapsulant chemistry and backsheet permeability govern moisture ingress and chemical aging, the pronounced increase in series resistance and the localized failure signatures observed in EL and DLIT imaging indicate that interconnect configuration and module assembly processes are critical contributors. Intrinsic differences between polycrystalline and monocrystalline silicon may influence crack morphology and defect propagation; however, under the present exposure conditions, the forensic evidence suggests that module-level design and material selection exert a stronger influence on long-term reliability than cell crystallography alone.

Ultimately, the degradation storyline derived here exemplifies how macroscopic power loss arises from microscopic material–environment interactions, offering quantitative insight for the design of next-generation encapsulants, adhesives, and metallization schemes aimed at 30-yr reliability targets.

4 Conclusions—future work

This fifteen-year field investigation draws upon one of the most comprehensive datasets on the long-term degradation of crystalline-silicon PV modules operated in a Mediterranean climate. Through the integration of continuous outdoor monitoring and laboratory forensics, the study establishes a direct causal chain linking macroscopic performance losses to microscopic material transformations.

At the system level, the polycrystalline-silicon modules degraded at an average rate of about 2.56%/year, more than three times the value generally assumed in warranties. Mono- and amorphous-silicon counterparts exhibited lower losses, underscoring the strong technology and climate dependence of PV reliability.

At the component level, multi-technique imaging (EL, UVFL, DLIT) and chemical analysis (fluorescence, FTIR) revealed that performance decline is governed by two intertwined degradation pathways:

- Optical attenuation, caused by the photo-oxidation of the EVA encapsulant and the formation of conjugated polyenes, leading to a uniform reduction of short-circuit current across all illumination levels.
- Electrical resistance growth, resulting from acetic-acid-driven corrosion and delamination at busbar and interconnect regions, which sharply increases series resistance and suppresses the fill factor—particularly under high irradiance.

These findings demonstrate that long-term reliability cannot be predicted by single-stress accelerated tests. The coupled effects of light, heat, and moisture—acting continuously over years—generate feedback mechanisms (chemical, electrical, and mechanical) that are not captured in conventional qualification sequences. The evidence of a locally preserved area under the aluminum-backed nameplate further proves that even modest diffusion barriers against moisture and oxygen can substantially extend module lifetime.

From a broader perspective, this work bridges the gap between outdoor performance data and material-level diagnostics, providing both empirical validation and boundary conditions for predictive lifetime models. The insights gained here directly inform encapsulant formulation, interconnect design, and backsheet architecture for next-generation, high-durability PV modules intended for 30-yr service lifetimes.

Key implications and recommendations that can also be concluded on the basis of this work include:

- **Material durability:** Reinforced encapsulants with lower acetic-acid formation potential and integrated moisture barriers should be prioritized in future designs.
- **Qualification testing:** Current IEC sequences underestimate coupled thermo-photo-hydrolytic stresses; adaptation toward multi-stress accelerated aging is required.
- **Predictive modelling:** The dataset provides benchmark values for calibrating degradation models linking optical transmission, series resistance, and yield loss.
- **Reliability monitoring:** Combining UV-fluorescence and electroluminescence offers an efficient diagnostic pair for early detection of encapsulant aging and interconnect failures.
- **Policy and warranties:** Long-term empirical data such as this are indispensable for refining warranty assumptions and de-risking PV investments.

In summary, real-field longevity remains the ultimate test of PV technology. By coupling continuous monitoring with forensic insight, this study not only quantifies

degradation but also explains it—offering a path toward more reliable, sustainable, and bankable solar power generation.

Future work will extend this approach toward more time-resolved diagnostic campaigns on additional long-term monitored PV arrays, enabling improved tracking of degradation kinetics and mechanism sequencing over time. Ongoing work focuses on extending the present analysis to a broader technology set, including modern PERC and TOPCon modules deployed under identical monitoring conditions. Additional efforts will integrate the electrical and chemical degradation indicators derived here into predictive lifetime models, enabling quantitative extrapolation of field behavior beyond the current 15-yr horizon. A complementary objective is to validate the observed encapsulant–interconnect degradation synergy across diverse climates and to assess mitigation strategies based on alternative encapsulant chemistries and barrier-film architectures.

Acknowledgments

Part of this work has been carried out in the framework of the Horizon Europe CACTUS and SUPERNOVA projects.

Funding

CACTUS project has received funding from the European Union’s Horizon Europe research and innovation programme under grant agreement No. 101132182. SUPERNOVA has received funding from the European Union’s Horizon Europe research and innovation programme under grant agreement No 101146883.

Also, part of this work was also supported by the French National Program “Programme d’Investissements d’Avenir - INES.2S” under Grant Agreement ANR-10-IEED-0014 0014-01.

Conflicts of interest

The authors have no conflicts of interest to disclose.

Data availability statement

Raw (source) monitoring data associated with this article cannot be publicly disclosed due to commercial and legal restrictions. Aggregated results and processed data supporting the findings of this study are included within the article. Specific datasets can be made available for scientific research purposes upon reasonable request to the corresponding author, subject to institutional approval.

Author contribution statement

Conceptualization: All authors; Methodology and Software: M. Babics and F. Mezzasalma; Measurements: L. Sicot, G. Capron, M. Babics, and J.-P. Rakotoniaina; Validation, Formal Analysis, and Data Curation: J.A. Tsanakas, M. Babics, H. Colin, P. Marechal, and J. Aimé; Resources, Supervision, Project Administration, and Funding Acquisition: J.A. Tsanakas and J. Aimé; Writing (Original Draft Preparation): J.A. Tsanakas, M. Babics, and A. Mignonac; Review and Editing: J.A. Tsanakas.

References

1. D.L.S. King, M.A. Quintana, J.A. Kratochvil, D.E. Ellibee, B. R. Hansen, Photovoltaic module performance and durability following long-term field exposure, *Prog. Photovolt. Res. Appl.* **8**, 241 (2008)
2. D.C. Jordan, S.R. Kurtz, Photovoltaic degradation rates—an analytical review, *Prog. Photovolt. Res. Appl.* **21**, 12 (2013). <https://doi.org/10.1002/pip.1182>
3. A. Phinikarides, N. Kindyni, G. Makrides, G.E. Georghiou, Review of photovoltaic degradation rate methodologies, *Renew. Sustain. Energy Rev.* **40**, 143 (2014)
4. M. Köntges, S. Kurtz, C. Packard, U. Jahn, K.A. Berger, K. Kato et al., Review of failures of photovoltaic modules, Report IEA-PVPS T13-01:2014
5. M. Köntges, G. Oreski, U. Jahn, M. Herz, P. Hacke, K.A. Weiss et al., Assessment of photovoltaic module failures in the field, Report IEA-PVPS T13-09:2017
6. U. Jahn, M. Herz, M. Köntges, D. Parlevliet, M. Paggi, I. Tsanakas et al., Review on infrared and electroluminescence imaging for PV field applications, Report IEA-PVPS T13-10:2018
7. M. Köntges, J. Lin, A. Virtuani, G.C. Eder, J. Zhu, G. Oreski et al., Reliability and performance of photovoltaic systems—degradation and failure modes in new photovoltaic cell and module technologies, Report IEA-PVPS T13-30:2025
8. C.R. Osterwald, T.J. McMahon, History of accelerated and qualification testing of terrestrial photovoltaic modules: a literature review, *Prog. Photovolt. Res. Appl.* **17**, 11 (2009). <https://doi.org/10.1002/pip.861>
9. V.P. Markevich, M. Vaquero-Contreras, J.T. De Guzman, J. Coutinho, P. Santos, I.F. Crowe et al., Boron-oxygen complex responsible for light-induced degradation in silicon photovoltaic cells: a new insight into the problem, *Phys. Status Solidi A* **216**, 1900315 (2019). <https://doi.org/10.1002/pssa.201900315>
10. M. Aghaei, A. Fairbrother, A. Gok, S. Ahmad, S. Kazim, K. Lobato et al., Review of degradation and failure phenomena in photovoltaic modules, *Renew. Sustain. Energy Rev.* **159**, 112160 (2022). <https://doi.org/10.1016/j.rser.2022.112160>
11. G. Oreski, B. Ottersböck, A. Omazic, Degradation processes and mechanisms of encapsulants, in: *Durability and Reliability of Polymers and Other Materials in Photovoltaic Modules* (Plastics Design Library, 2019), pp. 135-152. <https://doi.org/10.1016/B978-0-12-811545-9.00006-9>
12. G. Guerra, P. Mercade-Ruiz, G. Anamiati, L. Landberg, Long-term PV system modelling and degradation using neural networks, *EPJ Photovoltaics*. **14**, 30 (2023). <https://doi.org/10.1051/epjpv/2023018>
13. D.M. Atia, A.A. Hassan, H.T. El-Madany, A. Eliwa, M.B. Zahran, Degradation and energy performance evaluation of mono-crystalline photovoltaic modules in Egypt, *Sci. Rep.* **13**, 13066 (2023). <https://doi.org/10.1038/s41598-023-40168-8>
14. A. Skoczek, T. Sample, E.D. Dunlop, The results of performance measurements of field-aged crystalline silicon photovoltaic modules, *Prog. Photovolt. Res. Appl.* **17**, 227 (2009). <https://doi.org/10.1002/pip.874>
15. D. Polverini, M. Field, E. Dunlop, W. Zaaiman, Polycrystalline silicon PV modules performance and degradation over 20 yr, *Prog. Photovolt. Res. Appl.* **21**, 1004 (2013). <https://doi.org/10.1002/pip.2197>
16. M. Dhimish, Performance Ratio and Degradation Rate Analysis of 10-Yr Field Exposed Residential Photovoltaic Installations in the UK and Ireland, *Clean Technol.* **2**, 170 (2020). <https://doi.org/10.3390/cleantechnol2020012>
17. H.M. Shaik, A. Kabbani, A.M. Sheikh, K. Goh, N. Gupta, T. Umar, Measurement and validation of polysilicon photovoltaic module degradation rates over five years of field exposure in Oman, *AIMS Energy* **9**, 1192 (2021). <https://doi.org/10.3934/energy.2021055>
18. J. Denz, J. Hepp, C. Buerhop, B. Doll, J. Hauch, C.J. Brabec et al., Defects and performance of Si PV modules in the field—an analysis, *Energy Environ. Sci.* **15**, 2180 (2022). <https://doi.org/10.1039/D2EE00109H>
19. A.J. Curran, X. Yu, J. Liu, D.J. Colvin, N. Iqbal, T. Moran et al., Field studies of PERC and Al-BSF PV module performance loss using power and I-V timeseries, *Front. Energy Res.* **11**, 1127775 (2023). <https://doi.org/10.3389/fenrg.2023.1127775>
20. C. Schill, A. Anderson, C. Baldus-Jeursen, L. Burnham, L. Micheli, D. Parlevliet et al., Soiling losses—impact on the performance of photovoltaic power plants, Report IEA-PVPS T13-21:2022
21. R.R. Cordero, A. Damiani, D. Laroze, S. MacDonell, J. Jorquera, E. Sepulveda et al., Effects of soiling on photovoltaic (PV) modules in the Atacama Desert, *Sci. Rep.* **8**, 13943 (2018). <https://doi.org/10.1038/s41598-018-32291-8>
22. G. Badran, M. Dhimish, Field study on the severity of photovoltaic potential induced degradation, *Sci. Rep.* **12**, 22094 (2022). <https://doi.org/10.1038/s41598-022-26310-y>
23. I. Tsanakas, Aerial inspections and diagnostics of PV power plants, in: Focus Workshop on Operation & Maintenance, 2021 Sep 30
24. W. Herrmann, G.C. Eder, B. Farnung, G. Friesen, M. Köntges, B. Kubicek et al., Qualification of photovoltaic (PV) power plants using mobile test equipment, Report IEA-PVPS T13-24:2021
25. L. Koester, S. Lindig, A. Louwen, A. Astigarraga, G. Manzoloni, D. Moser, Review of photovoltaic module degradation, field inspection techniques and techno-economic assessment, *Renew. Sustain. Energy Rev.* **165**, 112616 (2022). <https://doi.org/10.1016/j.rser.2022.112616>
26. J.I.A. Tsanakas, P. Marechal, Decoding pixels: A modular software prototype for cognitive image-based diagnostics of PV plants, *EPJ Photovoltaics*, **16**, 24 (2025). <https://doi.org/10.1051/epjpv/2025013>
27. D.H. Daher, M. Aghaei, D.A. Quansah, M.S. Adaramola, P. Parvin, C. Ménéz. Multi-pronged degradation analysis of a photovoltaic power plant after 9.5 yr of operation under hot desert climatic conditions, *Prog. Photovolt. Res. Appl.* **31**, 888 (2023). <https://doi.org/10.1002/pip.3694>
28. M. Fuentes, M. Vivar, H. Hosein, J. Aguilera, E. Muñoz-Cerón, Lessons learned from the field analysis of PV installations in the Saharawi refugee camps after 10 yr of operation, *Renew. Sustain. Energy Rev.* **93**, 100 (2018). <https://doi.org/10.1016/j.rser.2018.05.019>

29. W. Luo, A.M. Khaing, C.D. Rodriguez-Gallegos, S.W. Leow, T. Reindl, M. Praveetoni, Long-term outdoor study of an organic photovoltaic module for building integration, *Prog. Photovolt. Res. Appl.* **32**, 481 (2024). <https://doi.org/10.1002/pip.3791>
30. S.C.S. Costa, L.L. Kazmerski, A.S.A.C. Diniz, Impact of soiling on Si and CdTe PV modules: case study in different Brazil climate zones, *Energy Convers. Manag. X* **10**, 100084 (2021). <https://doi.org/10.1016/j.ecmx.2021.100084>
31. S. Lindig, J. Deckx, M. Herz, J. Ascencio Vásquez, M. Theristis, B. Herteleer et al., Best practice guidelines for the use of economic and technical KPIs, Report IEA-PVPS T13-28:2024
32. M. Herz, G. Friesen, U. Jahn, M. Köntges, S. Lindig, D. Moser, Quantification of technical risks in PV power systems, IEA PVPS Task 13, Report IEA-PVPS T13-23:2021, 2021 Oct.
33. G. Friesen, M. Köntges, J. Lin, G. Oreski, G.C. Eder, P. Hacke et al., Photovoltaic failure fact sheets (PVFS)—Review 2025, Report IEA-PVPS T13-30:2025
34. A.W. Czanderna, F.J. Pern, Encapsulation of PV modules using ethylene vinyl acetate copolymer as a pottant: A critical review, *Sol. Energy Mater. Sol. Cells* **43**, 101 (1996). [https://doi.org/10.1016/0927-0248\(95\)00150-6](https://doi.org/10.1016/0927-0248(95)00150-6)
35. C. Buerhop-Lutz, O. Stroyuk, O. Mashkov, J.A. Hauch, I.M. Peters, Unveiling the potential of ultraviolet fluorescence imaging as a versatile inspection tool: Insights from extensive photovoltaic module inspections in multi-MWp photovoltaic power stations, *Sol. RRL* **8**, 2400566 (2024). <https://doi.org/10.1002/solr.202400566>
36. M. Köntges, A. Morlier, G. Eder, E. Fleis, B. Kubicek, J. Lin. Ultraviolet fluorescence as assessment tool for photovoltaic modules, *IEEE J. Photovolt.* **10**, 616 (2020). <https://doi.org/10.1109/JPHOTOV.2019.2961781>
37. P. Thornton, S.L. Moffitt, L.T. Schelhas, R.H. Dauskardt, Dependence of adhesion on degradation mechanisms of ethylene co-vinyl acetate encapsulants over the lifetime of photovoltaic modules, *Sol. Energy Mater. Sol. Cells* **244**, 111818 (2022). <https://doi.org/10.1016/j.solmat.2022.111818>
38. S. Uličná, A. Sinha, D.C. Miller, B.M. Habersberger, L.T. Schelhas, M. Owen-Bellini, PV encapsulant formulations and stress test conditions influence dominant degradation mechanisms, *Sol. Energy Mater. Sol. Cells* **255**, 112319 (2023). <https://doi.org/10.1016/j.solmat.2023.112319>

Cite this article as: J.A. Tsanakas, Maxime Babics, Frédéric Mezzasalma, Alexandre Mignonac, Hervé Colin, Lionel Sicot, Philippe Marechal, Guillaume Capron, Jean-Patrice Rakotoniaina, Jérémie Aimé, Long-term field degradation of crystalline-silicon PV modules: insights from fifteen years of monitoring and forensic analysis, *EPJ Photovoltaics* 17, 14 (2026), <https://doi.org/10.1051/epjpv/2026006>